

A 3D Coarse-to-Fine Framework for Automatic Pancreas Segmentation

Zhuotun Zhu¹, Yingda Xia¹, Wei Shen², Elliot K. Fishman³, Alan L. Yuille¹

¹ Department of Computer Science, The Johns Hopkins University, Baltimore, MD 21218, USA

² Shanghai University, Baoshan District, Shanghai 200444, China

³ School of Medicine, The Johns Hopkins University, Baltimore, MD 21287, USA

{zhuotun, philyingdaxia}@gmail.com, wei.shen@t.shu.edu.cn, efishman@jhmi.edu, alan.l.yuille@gmail.com

Abstract

In this paper, we adopt 3D CNNs to segment the pancreas in CT images. Although deep neural networks have been proven to be very effective on many 2D vision tasks, it is still challenging to apply them to 3D applications due to the limited amount of annotated 3D data and limited computational resources. We propose a novel 3D-based coarse-to-fine framework for volumetric pancreas segmentation to tackle these challenges. The proposed 3D-based framework outperforms the 2D counterpart to a large margin since it can leverage the rich spatial information along all three axes. We conduct experiments on two datasets which include healthy and pathological pancreases respectively, and achieve the state-of-the-art in terms of Dice-Sørensen Coefficient (DSC). Moreover, the worst case of DSC on the NIH dataset was improved by 7% to reach almost 70%, which indicates the reliability of our framework in clinical applications.

1. Introduction

Driven by the huge demands for computer-aided diagnosis systems, automatic organ segmentation from medical images, such as computed tomography (CT) and magnetic resonance imaging (MRI), has become an active research topic in both the medical image processing and computer vision communities. It is a prerequisite step for many clinical applications, such as diabetes inspection, organic cancer diagnosis, and surgical planning. Due to the insufficient number of experienced doctors and limited working efficiency, pancreatic cancers were the 7th most common cause of cancer deaths in 2012 globally [27]. Therefore, it is well worth exploring automatic segmentation systems to accelerate the computer-aided diagnosis in medical image analysis.

In this paper, we focus on pancreas segmentation from CT scans, one of the most challenging organ segmentation problems. As shown in Fig. 1, the main difficulties stem from three aspects: 1) the small size of the pancreas in the

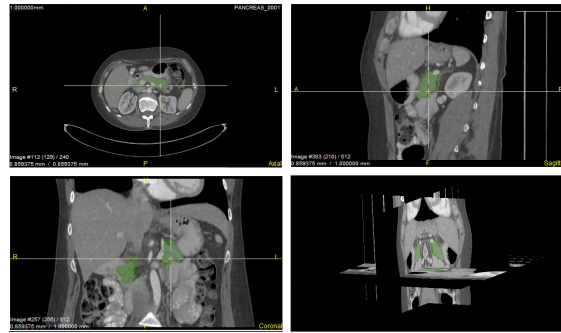


Figure 1: An illustration of the pancreas organ shown in a 3D space on the bottom right as well as three views (axial, sagittal and coronal planes on the upper-left, upper-right and lower-left, respectively) on the NIH dataset [23]. Note that the pancreas regions are masked as light green while all other organs are in gray scale. We can find that the pancreas organ occupies a relatively small region inside a whole 3D CT scan. Best viewed in color.

whole abdominal CT volume; 2) the large variations in texture, location, shape and size of the pancreas; 3) the significant ambiguities along the boundaries between pancreatic and non-pancreatic tissues. In the supplementary material, we put more examples to illustrate the three difficulties.

Following the rapid development of deep neural networks [14, 26] and their successes in many computer vision tasks, such as semantic segmentation [17, 4], edge detection [25, 28] and 3D shape retrieval [33, 7], many deep learning based methods have been proposed for pancreas segmentation and achieved considerable progress [23, 24, 32]. However, these methods are based on 2D fully convolutional networks (FCNs) [17], which perform segmentation slice by slice while CT volumes are indeed 3D data. Although these 2D methods use strategies to fuse the output from different 2D views to obtain 3D segmentation results, they inevitably lose some 3D context, which is important for capturing the discriminative features of the pancreas with respect to background regions.

Using 3D deep networks for organ segmentation is a recent trend but not yet applied to the pancreas. An obstacle is that training 3D deep networks suffers from the “out of memory” problem. 2D FCNs can accept a whole 2D slice as input, but 3D FCNs cannot be fed a whole 3D volume due to the limited GPU memory size. A common solution is to train 3D FCNs from small sub-volumes and test them in a sliding-window [19, 1, 5, 3, 29], *i.e.*, performing 3D segmentation on densely and uniformly sampled sub-volumes one by one. Usually, these neighboring sampled sub-volumes overlap with each other to improve the robustness of the final 3D results. It is worth noting that the overlap size is a trade-off between the segmentation accuracy and the time cost. Setting a larger/smaller overlap size generally leads to a better/worse segmentation accuracy but takes more/less time during testing.

To address these issues, we propose a concise and effective framework based on 3D deep networks for pancreas segmentation, which can simultaneously achieve high segmentation accuracy and low time cost. Our framework is formulated in a coarse-to-fine manner. In the training stage, we first train a 3D FCN from the sub-volumes sampled from an entire CT volume. We call this *ResDSN Coarse* model, which aims to obtain the rough location of the target pancreas from the whole CT volume by making full use of the overall 3D context. Then, we train another 3D FCN from the sub-volumes sampled only from the ground truth bounding boxes of the target pancreas. We call this the *ResDSN Fine* model, which can refine the segmentation based on the coarse result. In the testing stage, we first apply the coarse model in the sliding-window to a whole CT volume to extract the most possible location of the pancreas. Since we only need a rough location for the target pancreas in this step, the overlap size is set to a small value. Afterwards, we apply the fine model in the sliding-window manner to the coarse pancreas region, but by setting a larger overlap size. Thus, we can efficiently obtain a fine segmentation result and we call the coarse-to-fine framework by *ResDSN C2F*.

Besides the efficient inference, another advantage for applying this coarse-to-fine framework to pancreases segmentation is that the coarse step removes a large amount of the unrelated background region, which can improve the accuracy in the fine stage. Recall that a pancreas only takes up a small fraction of an entire abdominal CT volume. With a relatively smaller region to be sampled as input, the fine step learns cues which distinguish the pancreas from the local background, *i.e.*, exploit local context which makes it easier to obtain a more accurate segmentation result.

To our best knowledge, we are the first to segment the challenging pancreas using 3D networks which leverage the rich spatial information. The effectiveness and efficiency of the proposed 3D coarse-to-fine framework are demonstrated on two pancreas segmentation datasets where we achieve

the state-of-the-art with relative low time cost.

2. Related Work

The medical image analysis community is facing a revolution brought by the fast development of deep networks [14, 26]. Deep Convolutional Neural Networks (CNNs) based methods have dominated the research area of volumetric medical image segmentation in the last few years. Generally speaking, CNN-based methods for volumetric medical image segmentation can be divided into two major categories: 2D CNNs based and 3D CNNs based.

2.1. 2D CNNs for Volumetric Segmentation

2D CNNs based methods [10, 23, 24, 20, 22] performed volumetric segmentation slice by slice from different views, and then fused the 2D segmentation results to obtain a 3D Volumetric Segmentation result. In the early stage, the 2D segmentation based models were trained from image patches and tested in a patch by patch manner [23], which is time consuming. Since the introduction of fully convolution networks (FCNs) [17], almost all the 2D segmentation methods are built upon 2D FCNs to perform holistic slice segmentation during both training and testing. Havaei *et al* [10] proposed a two-pathway FCN architecture, which exploited both local features as well as more global contextual features simultaneously by the two pathways. Roth *et al* [24] performed Pancreas segmentation by a holistic learning approach, which first segment pancreas regions by holistically-nested networks [28] and then refine them by the boundary maps obtained by robust spatial aggregation using random forest. The U-Net [22] is one of the most popular FCN architectures for medical image segmentation, which is a encoder-decoder network, but with additional short connection between encoder and decoder paths. Based on the fact that a pancreas only takes up a small fraction of the whole scan, Zhou *et al.* [32] proposed to find the rough pancreas region and then learn a FCN based fixed-point model to refine the pancreas region iteratively.

2.2. 3D CNNs for Volumetric Segmentation

Although 2D CNNs based methods achieved considerable progresses, but they are not optimal for medical image segmentation, as they cannot make full use of the 3D context encoded in volumetric data. Several 3D CNNs based segmentation methods have been proposed. The 3D U-Net [5] extended the previous 2D U-Net architecture [22] by replacing all 2D operations with their 3D counterparts. Based on the architecture of the 3D U-Net, the V-Net [19] introduced residual structures [11] (short term skip connection) into each stage of the network. Chen *et al* [3] proposed a deep voxel-wise residual network for 3D brain segmentation. Both I2I-3D [18] and 3D-DSN [6] included auxiliary supervision via side outputs into their 3D deep networks.

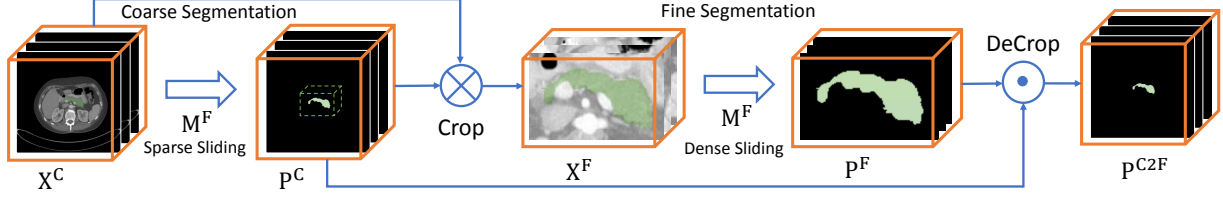


Figure 2: Flowchart of the proposed 3D coarse-to-fine segmentation system in the testing phase. We first apply “ResDSN Coarse” with a sparse sliding window to obtain a rough pancreas region and then use the “ResDSN Fine” model to refine the results with a dense sliding window. Best viewed in color.

3. Method

In this section, we elaborate our proposed 3D coarse-to-fine framework which includes a *coarse* stage and a *fine* stage afterwards. We first formulate a segmentation model that can be generalized to both *coarse* stage and *fine* stage. Later in Sec. 3.1 and Sec. 3.2, we will customize the segmentation model to these two stages, separately.

We denote a 3D CT-scan volume by \mathbf{X} . This is associated with a human-labeled per-voxel annotation \mathbf{Y} , where both \mathbf{X} and \mathbf{Y} have size $W \times H \times D$, which corresponds to axial, sagittal and coronal views, separately. The ground-truth segmentation mask \mathbf{Y} has a binary value y_i , $i = 1, \dots, WHD$, at each spatial location i where $y_i = 1$ indicates that x_i is a pancreas voxel. Denote a segmentation model by $\mathbb{M} : \mathbf{P} = \mathbf{f}(\mathbf{X}; \Theta)$, where Θ indicates model parameters and \mathbf{P} means the binary prediction volume. Specifically in a neural network with L layers and parameters $\Theta = \{\mathcal{W}, \mathcal{B}\}$, \mathcal{W} is a set of weights and \mathcal{B} is a set of biases, where $\mathcal{W} = \{\mathbf{W}^1, \mathbf{W}^2, \dots, \mathbf{W}^L\}$ and $\mathcal{B} = \{\mathbf{B}^1, \mathbf{B}^2, \dots, \mathbf{B}^L\}$. Given that $p(y_i|x_i; \Theta)$ represents the predicted probability of a voxel x_i being what is the labeled class at the final layer of the output, the negative log-likelihood loss can be formulated as:

$$\mathcal{L}(\mathbf{X}; \Theta) = - \sum_{x_i \in \mathbf{X}} \log(p(y_i|x_i; \Theta)). \quad (1)$$

It is also known as the cross entropy loss in our binary segmentation setting. By thresholding $p(y_i|x_i; \Theta)$, we can obtain the binary segmentation mask \mathbf{P} .

We also add some auxiliary layers to such a neural network (will be called mainstream network in the rest of the paper), which produces side outputs under deep supervision [16]. These auxiliary layers form a branch network and facilitate the feature learning at lower layer of the mainstream network. Each branch network shares the weights of the first d layers from the mainstream network, which is denoted by $\Theta_d = \{\mathcal{W}_d, \mathcal{B}_d\}$. Apart from the shared weights, it owns weights $\hat{\Theta}_d$ to output the per-voxel prediction. Sim-

ilarly, the loss of an auxiliary network can be formulated as:

$$\mathcal{L}_d(\mathbf{X}; \Theta_d, \hat{\Theta}_d) = - \sum_{x_i \in \mathbf{X}} \log(p(y_i|x_i; \Theta_d, \hat{\Theta}_d)). \quad (2)$$

Finally, stochastic gradient descent is applied to minimize the negative log-likelihood to fit parameters to a dataset, which is given by the following overall objective function:

$$\mathcal{L} = \mathcal{L}(\mathbf{X}; \Theta) + \sum_{d \in \mathcal{D}} \xi_d \mathcal{L}_d(\mathbf{X}; \Theta_d, \hat{\Theta}_d) + \lambda (\|\Theta\|^2 + \sum_{d \in \mathcal{D}} \|\hat{\Theta}_d\|^2), \quad (3)$$

where \mathcal{D} is a set of branch networks for auxiliary supervisions, ξ_d balances the importance of each auxiliary network and l_2 regularization is added to the objective to prevent the networks from overfitting. For conciseness concerns in the following sections, we keep a segmentation model that is obtained from the overall function described in Eq. 3 denoted by $\mathbb{M} : \mathbf{P} = \mathbf{f}(\mathbf{X}; \Theta)$, where Θ includes parameters of the mainstream network and auxiliary networks.

3.1. Coarse Stage

In the *coarse* stage, the input of “ResDSN Coarse” is sampled from the whole CT-scan volume denoted by \mathbf{X}^C , on which the *coarse* segmentation model $\mathbb{M}^C : \mathbf{P}^C = \mathbf{f}^C(\mathbf{X}^C; \Theta^C)$ is trained on. All the C superscripts depict the *coarse* stage. The goal of this stage is to efficiently produce a rough binary segmentation \mathbf{P}^C from the complex background, which can get rid of regions that are segmented as non-pancreas with a high confidence to obtain an approximate pancreas volume. Based on this approximate pancreas volume, we can crop from the original input \mathbf{X}^C with a rectangular cube derived from \mathbf{P}^C to obtain a smaller 3D image space \mathbf{X}^F , which is surrounded by simplified and less variable context compared with \mathbf{X}^C . The mathematic definition of \mathbf{X}^F is formulated as:

$$\mathbf{X}^F = \text{Crop}[\mathbf{X}^C \otimes \mathbf{P}^C; \mathbf{P}^C], \quad (4)$$

where \otimes means an element-wise product. The function $\text{Crop}[\mathbf{X}; \mathbf{P}]$ denotes cropping \mathbf{X} via a rectangular cube that covers all the 1’s voxels of a binary volume \mathbf{P} added by a

padding margin m along three axes. Given \mathbf{P} , the functional constraint imposed on \mathbf{X} is that they have exactly the same dimensionality in 3D space. The padding parameter m is empirically determined in experiments, where it is used to better segment the boundary voxels of pancreas during the *fine* stage. The Crop operation acts as a dimensionality reduction to facilitate the fine segmentation, which is crucial to cut down the consuming time of segmentation. It is well-worth noting that the 3D locations of the rectangular cube which specifies where to crop \mathbf{X}^F from \mathbf{X}^C is recorded to map the *fine* segmentation results back their positions in the full CT scan.

3.2. Fine Stage

In the *fine* stage, the input of the ConvNet is sampled from the cropped volume \mathbf{X}^F , on which we train the *fine* segmentation model $\mathbb{M}^F : \mathbf{P}^F = \mathbf{f}^F(\mathbf{X}^F; \Theta^F)$, where the F superscripts indicate the *fine* stage. The goal of this stage is to refine the coarse segmentation results from previous stage. In practice, \mathbf{P}^F has the same volumetric size of \mathbf{X}^F , which is smaller than the original size of \mathbf{X}^C .

3.3. Coarse-to-Fine Segmentation

Our segmentation task is to give a volumetric prediction on every voxel of \mathbf{X}^C , so we need to map the \mathbf{P}^F back to exactly the same size of \mathbf{X}^C given by:

$$\mathbf{P}^{C2F} = \text{DeCrop}[\mathbf{P}^F \odot \mathbf{P}^C; \mathbf{X}^F, \mathbf{X}^C], \quad (5)$$

where \mathbf{P}^{C2F} denotes the final volumetric segmentation, and DeCrop operation defined on $\mathbf{P}^F, \mathbf{P}^C, \mathbf{X}^F$ and \mathbf{X}^C is to replace a pre-defined rectangular cube inside \mathbf{P}^C by \mathbf{P}^F , where the replacement locations are given by the definition of cropping \mathbf{X}^F from \mathbf{X}^C given in Eq. 4.

All in all, our entire 3D-based coarse-to-fine segmentation framework during testing is illustrated in Fig 2.

3.4. Network Architecture

As shown in Fig. 3, we provide an illustration of our convolutional network architecture. Inspired by 3D U-Net [5], V-Net [19] and VoxResNet [3], we have an encoder path on the left and a decoder path on the right each with four resolution steps. The left part of network acts as a feature extractor to learn higher and higher level of representations while the right part of network decompresses compact features into finer and finer resolution to predict the per-voxel segmentation. The padding and stride of each layer (Conv, Pooling, DeConv) are carefully designed to make sure the densely predicted output is the same size as the input.

The encoder sub-network on the left is divided into different steps that work on different resolutions. Each step consists of one to two convolutions, where each convolution is composed of $3 \times 3 \times 3$ convolution followed by a

batch normalization (BN [12]) and a rectified linear unit (ReLU [21]) to reach better convergence, and then a max pooling layer with a kernel size of $2 \times 2 \times 2$ and strides of two to reduce resolutions and learn more compact features. The downsampling operation implemented by max-pooling can reduce the size of the intermediate feature maps while increasing the size of the receptive fields. Having fewer size of activations makes it possible to double the number of channels than one of the previous layer during feature aggregation because of the limited computational resource.

The decoder sub-network on the right is composed of several steps that operate on different resolutions as well. Each step has two convolutions with each one followed by a BatchNorm and a ReLU, and afterwards a Deconvolution with a kernel size of $4 \times 4 \times 4$ and strides of two is connected to expand the feature maps and finally predict the segmentation mask at the last layer. The upsampling operation that is carried out by deconvolution enlarges the resolution between each step, which increases the size of the intermediate activations so that we need to halve the number of channels due to the limited memory of the GPU card.

Apart from the left and right sub-networks, we impose a residual connection [11] to bridge short-cut connections of features between low-level layers and high-level layers. During the forward phase, the low-level cues extracted by networks are directly added to the high-level cues, which can help elaborate the fine-scaled segmentation, *e.g.*, small parts close to the boundary which may be ignored during the feature aggregation due to the large size of receptive field at high-level layers. As for the backward phase, the supervision cues at high-level layers can be back-propagated through the short-cut way via the residual connections. This type of mechanism can prevent networks from gradient vanishing and exploding [8], which hampers network convergence during training.

We have one mainstream loss layer connected from “Res/Conv1b” and another two auxiliary loss layers connected from “Conv2b” and “Conv3b” to the ground truth label, respectively. For the mainstream loss in “Res/Conv1b” as the last layer which has the same size of data flow as one of the input, a $1 \times 1 \times 1$ convolution is followed to reduce the number of channels to the number of label classes which is 2 in our case. As for the two auxiliary loss layers, deconvolution layers are connected to upsample feature maps to be the same as input.

The deep supervision imposed by auxiliary losses provides robustness to hyper-parameters choice, in that the low-level layers are guided by the direct segmentation loss, leading to faster convergence rate. Throughout this work, we have two auxiliary branches where the default parameters are $\xi_1 = 0.2$ and $\xi_2 = 0.4$ in Eq. 3 to control the importance of deep supervisions compared with the major supervision from the mainstream loss for all segmentation

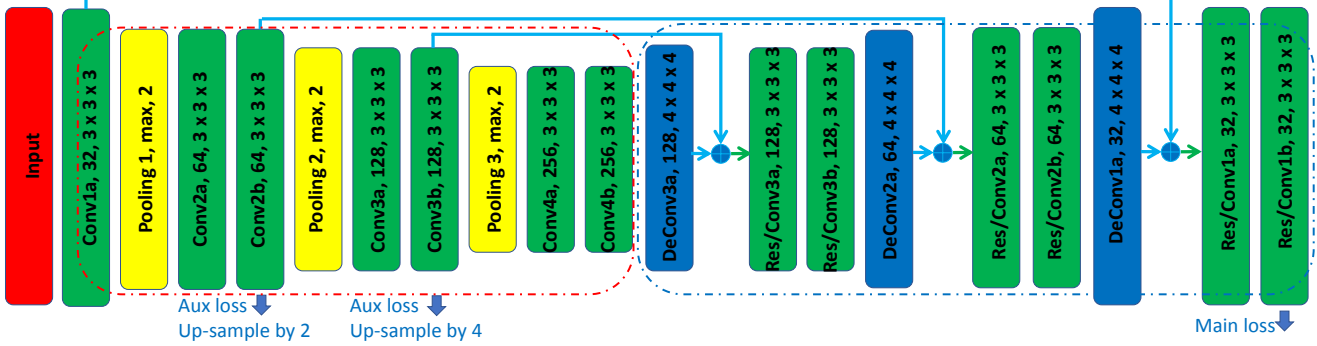


Figure 3: Illustration of the backbone network architecture of our 3D based convolutional neural network for volumetric segmentation. Each convolution or deconvolution layer consists of one convolution followed by a BatchNorm and a ReLU. To clarify, “Conv1a, 32, $3 \times 3 \times 3$ ” means the convolution operation with the number of channels as 32 and a kernel size of $3 \times 3 \times 3$. “Pooling 1, max, 2” means the max pooling operation with kernel size of $2 \times 2 \times 2$ and a stride of two. Blue concrete line with arrow in the end denotes the long-residual connection. Red dashed lines circle the encoder path while blue dashed lines circle the decoder path. Best viewed in color.

Method	Long Res	Short Res	Deep Super	Loss
ResDSN (Ours)	Sum	No	Yes	CE
FResDSN	Sum	Sum	Yes	CE
SResDSN	No	Sum	Yes	CE
3D U-Net [5]	Concat	No	No	CE
V-Net [19]	Concat	Sum	No	DSC
VoxResNet [3]	No	Sum	Yes	CE
MixedResNet [30]	Sum	Sum	Yes	CE
3D DSN [6]	No	No	Yes	CE
3D HED [18]	Concat	No	Yes	CE

Table 1: Configurations comparison of different 3D segmentation networks on medical image analysis. For all the abbreviated phrases, “Long Res” means long residual connection, “Short Res” means short residual connection, “Deep Super” means deep supervision implemented by auxiliary loss layers, “Concat” means concatenation, “DSC” means Dice-Sørensen Coefficient and “CE” means cross-entropy. For residual connection, it has two types: concatenation (“Concat”) or element-wise sum (“Sum”).

networks unless stated otherwise.

As shown in Table 1, we give the detailed comparisons of network configurations in terms of four aspects: long residual connection, short residual connection, deep supervision and loss function. Our backbone network architecture, named as “ResDSN”, is proposed with different strategies in terms of combinations of long residual connection and short residual connection compared with VoxResNet [3], MixedResNet [30], 3D DSN [6] and 3D HED [18]. In this table, we also depict “FResDSN” and “SResDSN”, where “FResDSN” and “SResDSN” are similar to MixedResNet [30] and VoxResNet [3], respectively. As confirmed by our quantitative experiments in Sec. 5.2, instead of adding short residual connections to the network, *e.g.*, “FResDSN” and “SResDSN”, we only choose the long residual element-wise sum, which can be more compu-

tationally efficient while even performing better than the “FResDSN” architecture which is equipped with both long and short residual connections. Moreover, ResDSN has noticeable differences with respect to the 3D U-Net [5] and V-Net [19]. On the one hand, compared with 3D U-Net and V-Net which concatenate the lower-level local features to higher-level global features, we adopt the element-wise sum between these features, which outputs less number of channels for efficient computation. On the other hand, we introduce deep supervision via auxiliary losses into the network to yield better convergence.

V-Net [19] introduces a new objective function, which aims to directly optimize the Dice coefficient formulated as: $2 \sum_i^{WHD} p_i y_i / (\sum_i^{WHD} p_i^2 + \sum_i^{WHD} y_i^2)$ given the ground truth y_i and the corresponding binary prediction p_i across every spatial position i . The main reason that we do not use Dice loss for training is that it only has gradients on the pancreas positions, which throws away patches without any pancreas voxels, *i.e.*, negative patches, leading to many false positive predictions if we are using a sliding window for both training and testing phases.

4. Experiments

In this section, we first describe in detail how we conduct training and testing in the *coarse* and *fine* stages, respectively. Then we are going to compare our proposed method with previous state-of-the-art on two pancreas datasets: NIH dataset [23] and JHMI pathological dataset [31].

4.1. Network Training and Testing

All our experiments were run on a desktop equipped with the NVIDIA TITAN X (Pascal) GPU and deep neural networks were implemented based on the Caffe [13] platform customized to support 3D operations for all necessary layers, *e.g.*, “convolution”, “deconvolution” and “pooling”,

etc. For the data pre-processing, we simply truncated the raw intensity values to be in $[-100, 240]$ and then normalized all raw CT cases to have zero mean and unit variance to decrease the data variance caused by the physical processes [9] of medical images. As for the data augmentation in the training phase, unlike sophisticated processing used by others, e.g., elastic deformation [19, 22], we utilized simple but effective augmentations, i.e., rotation (90° , 180° , and 270°) and flip in all three axes (axial, sagittal and coronal), to increase the number of 3D cases which can alleviate the scarce of CT scans with expensive human annotations. Note that different CT cases have different physical resolutions but we keep their resolutions unchanged. The input size of all our networks is denoted by $W_I \times H_I \times D_I$, where $W_I = H_I = D_I = 64$ in this paper.

For the *coarse* stage, we randomly sampled $64 \times 64 \times 64$ sub-volumes from the whole CT scan in the training phase. In this case, a sub-volume can either cover a portion of pancreas voxels or be cropped from regions with non-pancreas voxels at all, which acts as a hard negative mining to reduce the false positive. In the testing phase, a sliding window was carried out to the whole CT volume with a *coarse* stepsize that has small overlaps within each neighboring sub-volume. Specifically, for a testing volume with a size of $W \times H \times D$, we have a total number of $(\lfloor \frac{W}{W_I} \rfloor + n) \times (\lfloor \frac{H}{H_I} \rfloor + n) \times (\lfloor \frac{D}{D_I} \rfloor + n)$ sub-volumes to be fed into the network and then combined to obtain the final prediction, where n is a parameter to control the sliding overlaps that a larger n results in a larger overlap and vice versa. In the *coarse* stage for the low time cost concern, we set $n = 6$ to efficiently locate the rough region of pancreas \mathbf{X}^F defined in Eq. 4 from the whole CT scan \mathbf{X}^C .

For the *fine* stage, we randomly cropped $64 \times 64 \times 64$ sub-volumes constrained to be from the pancreas regions defined by ground-truth labels during training. In this case, a training sub-volume was assured to cover pancreatic voxels, which was specifically designed to be capable of segmentation refinement. In the testing phase, we only applied the sliding window on \mathbf{X}^F with a size of $W_F \times H_F \times D_F$. The total number of sub-volumes to be tested is $(\lfloor \frac{W_F}{W_I} \rfloor + n) \times (\lfloor \frac{H_F}{H_I} \rfloor + n) \times (\lfloor \frac{D_F}{D_I} \rfloor + n)$. In the *fine* stage for the high accuracy performance concern, we set $n = 12$ to accurately estimate the pancreatic mask \mathbf{P}^F from the rough segmentation volume \mathbf{X}^F . In the end, we mapped the \mathbf{P}^F back to \mathbf{P}^C to obtain \mathbf{P}^{C2F} for the final pancreas segmentation as given in Eq. 5, where the mapping location is given by the cropped location of \mathbf{X}^F from \mathbf{X}^C .

After we get the final binary segmentation mask, we denote \mathcal{P} and \mathcal{Y} to be the set of pancreas voxels in the prediction and ground truth, separately, i.e., $\mathcal{P} = \{i | p_i = 1\}$ and $\mathcal{Y} = \{i | y_i = 1\}$. The evaluation metric is defined by the Dice-Sørensen Coefficient (DSC) formulated as $\text{DSC}(\mathcal{P}, \mathcal{Y}) = \frac{2 \times |\mathcal{P} \cap \mathcal{Y}|}{|\mathcal{P}| + |\mathcal{Y}|}$. This evaluation measurement

Method	Mean DSC	Max DSC	Min DSC
ResDSN C2F (Ours)	84.59 ± 4.86%	91.45%	69.62%
ResDSN Coarse (Ours)	83.18 ± 6.02%	91.33%	58.44%
Cai <i>et al.</i> [2]	82.4 ± 6.7%	90.1%	60.0%
Zhou <i>et al.</i> [32]	82.37 ± 5.68%	90.85%	62.43%
Dou ¹ <i>et al.</i> [6]	82.25 ± 5.91%	90.32%	62.53%
Roth <i>et al.</i> [24]	78.01 ± 8.20%	88.65%	34.11%
Yu ¹ <i>et al.</i> [29]	71.96 ± 15.34%	89.27%	0%
Roth <i>et al.</i> [23]	71.42 ± 10.11%	86.29%	23.99%

Table 2: Evaluation of different methods on the NIH pancreas segmentation dataset. Our proposed framework achieves the state-of-the-art by a large margin compared with previous state-of-the-art.

ranges in $[0, 1]$ where 1 means a perfect prediction.

4.2. NIH

We conduct experiments on the NIH pancreas segmentation dataset [23], which contains 82 contrast-enhanced abdominal CT volumes provided by an experienced radiologist. The size of CT volumes is $512 \times 512 \times D$, where $D \in [181, 466]$ and their spatial resolutions are $w \times h \times d$, where $d = 1.0\text{mm}$ and $w = h$ that ranges from 0.5mm to 1.0mm . Data pre-processing and data augmentation were described in Sec. 4.1. Note that we did not normalize the spatial resolution into the same one since we wanted to impose the networks to learn to deal with the variations between different volumetric cases. Following the training protocol [23], we perform 4-fold cross-validation in a random split from 82 patients for training and testing folds, where each testing fold has 21, 21, 20 and 20 cases, respectively. We trained networks illustrated in Fig. 3 with a base learning rate to be 0.01 via polynomial decay (the power is 0.9) in a total of 80,000 iterations, and the weight decay parameter was set to be 0.0005 with a 0.9 momentum. Both training networks in the *coarse* and *fine* stages shared the same training parameter settings except that they took a $64 \times 64 \times 64$ input sampled from different underlying distributions described in Sec. 4.1, which included the details of testing settings as well. We average the score map of overlapped regions from the sliding window and throw away small isolated predictions whose portions are smaller than 0.2 of the total prediction. For DSC evaluation, we report the average with standard deviation, max and min statistics over all 82 testing cases as shown in Table 2.

First of all, our overall coarse-to-fine framework outperforms previous state-of-the-art by nearly 2.2% (Cai *et al.* [2] and Zhou *et al.* [32]) in terms of average DSC, which is a large improvement. The lower standard deviation of DSC shows that our method is the most stable and robust

¹The results are reported by our runs using the same cross-validation splits where code is available from their GitHub: <https://github.com/yulequan/HeartSeg>.

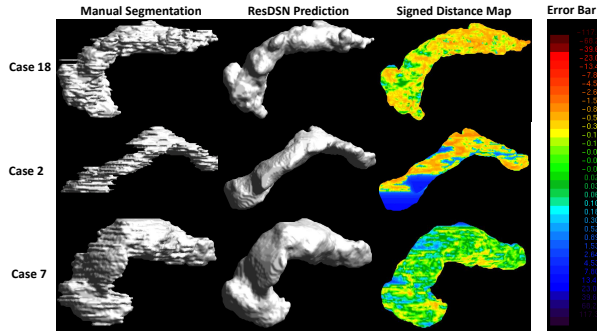


Figure 4: An illustration the predicted segmentation of our framework on NIH dataset. In the third column which shows the signed distance map between manual segmentation and ResDSN prediction, green regions means a perfect prediction while yellow and blue denote under-estimation and over-estimation, respectively. Best viewed in color.

across all different CT cases. Although the enhancement of max DSC of our framework is small due to the saturation, the improvement of min DSC over the second best (Dou *et al.* [6]) is from 62.53% to 69.62%, which is a more than 7% advancement. The worst case almost reaches 70%, which is a reasonable and acceptable segmentation result. After coarse-to-fine, the segmentation result of the worst case was improved by more than 11% after the 3D-based refinement from the 3D-based coarse result. The overall average DSC was also improved by 1.41%, which proves the effectiveness of our framework.

As shown in Fig 4, we display three segmentation examples of our “ResDSN” in comparison with the manual ground truth each case shown in one row. First of all, our ResDSN outputs a 3D segmentation with a very natural and smooth boundary while the manual segmentation is jagged to some extent since the annotation was labeled slice by slice. For the case 2, it seems that our ResDSN has a very large over-estimation at the pancreas head (left bottom region) but we got confirmed from experienced radiologists that our prediction should be correct while the over-estimation is caused by a missing annotation. For the case 7, ResDSN gives an almost perfect segmentation; and for the case 18, the predicted result shows more under-estimation.

4.3. JHMI

We applied our framework on the JHMI pathological cyst dataset [31] of abdominal CT scans. Different from the NIH healthy pancreas dataset, this dataset includes pathological cysts where some can be or can become cancerous. The pancreatic cancer stage largely influences the morphology of the pancreas [15] that makes this dataset extremely challenging for considering the large variants.

This dataset has a total number of 131 contrast-enhanced

Method	Mean DSC
ResDSN C2F (Ours)	80.56 ± 13.36%
ResDSN Coarse (Ours)	77.96 ± 13.36%
Zhou <i>et al.</i> [31]	79.23 ± 9.72%

Table 3: Evaluations on the JHMI pathological pancreas.

abdominal CT volumes with human-labeled pancreas annotations. The size of CT volumes is $512 \times 512 \times D$, where $D \in [358, 1121]$ that spans a wider variety of thickness than one of the NIH dataset. Following the training protocol [31], we conducted 4-fold cross validation on this dataset where each testing fold has 33, 33, 32 and 33 cases, respectively. We trained networks illustrated in Fig. 3 in both the *coarse* and *fine* stage with the same training settings as on the NIH except that we trained a total of 300,000 iterations on this pathological dataset since a pancreas with cysts is more difficult to segment than a normal case. In the testing phase, we vote the prediction map of overlapped regions from the sliding window and ignore small isolated pancreas predictions whose portions are smaller than 0.05 of the total prediction. As shown in Table. 3, we compare our framework with only one available published results on this dataset. “ResDSN C2F” achieves an average 80.56% DSC that consistently outperforms the 2D based coarse-to-fine method [31], which confirms the advantage of leveraging the rich spatial information along three axes. What’s more, the “ResDSN C2F” improves the “ResDSN Coarse” by 2.60% in terms of the mean DSC, which is a remarkable improvement that proves the effectiveness of the proposed 3D coarse-to-fine framework.

5. Discussion

In this section, we discuss the under-estimation versus over-estimation, residual connection and time efficiency to further investigate the effectiveness and efficiency of our proposed framework for pancreas segmentation.

5.1. Under-estimation and Over-estimation

We reproduced the 2D-based coarse-to-fine method (Zhou² *et al.* [32], abbreviated by “2D C2F”) which is the previous state-of-the-art on the NIH dataset. In comparison within “2D C2F”, our “ResDSN C2F” and “ResDSN Coarse” as displayed in Fig 5, we plotted a scatter graph to show the relation of *under-estimation* and *over-estimation* and the DSC score of each case. The under-estimation means that the ground truth voxel belongs to a pancreas while the segmentation model disagrees, and the over-estimation is defined as vice versa. Each red line with

²The code is available from their project webpage: <http://lingxixie.com/Projects/OrganSegC2F.html>. We reproduced the DSC of $82.18 \pm 6.72\%$ on the NIH dataset.

a -1 slope indicates all case points with the same DSC while the only violet line with an 1 slope (referred to as **DSC Equivalence Line**) indicates all cases whose number of under-estimation points is the same with one of over-estimation points. On the one hand, we can find from the left sub-figure that our 3D-based “ResDSN Coarse” pushes the DSC to a better performance (points are closer to the origin where the DSC is higher) compared with the “2D C2F”, which confirms the advantage of training a 3D network in the natural 3D CT data over 2D networks. We hypothesize that the advantage acquired by training 3D networks is that it can harness the rich spatial information via all 3D operations, *e.g.*, 3D convolution/deconvolution kernels and pooling operations, which are tailored to 3D tasks, *i.e.*, 3D CT pancreas segmentation in this work. On the other hand, we compare our 3D coarse-to-fine “ResDSN C2F” with “ResDSN Coarse” which is before refinement of the *fine* stage on the right sub-figure. A worthwhile observation is that cases points (green dots) of “ResDSN Coarse” severely tend to be spread on the upper-left region of the **DSC Equivalence Line**, which means the pancreas segmentation of “ResDSN” in the *coarse* stage is observed with a tendency to under-estimation. This observation experimentally strengthens the necessary step of refinement after coarse segmentation. As shown from the right sub-figure, cases points (red stars) after refinement are adjusted to the origin and distributed in better balance besides the **DSC Equivalence Line**, in which case the under-estimation issue is alleviated after our proposed coarse-to-fine framework.

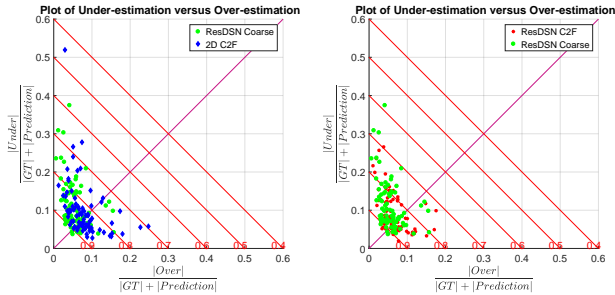


Figure 5: Illustration of different methods in terms of the comparison between under-estimation and over-estimation. The red line with a red number at the end of the line means the positions where the DSC score is indicated by red numbers. Best viewed in color.

5.2. Residual Connection

We discuss how different combinations of residual connections contribute to the pancreas segmentation task on the NIH dataset. All the residual connections are implemented in the element-wise sum and they shared exactly the same deep supervision connections, cross-validation splits, data input, training and testing settings except that the residual structure is different from each other. As given in Table. 4,

Method	Mean DSC	Max DSC	Min DSC
ResDSN Coarse (Ours)	83.18 ± 6.02%	91.33%	58.44%
FResDSN Coarse	83.11 ± 6.53%	91.34%	61.97%
SResDSN Coarse	82.82 ± 5.97%	90.33%	62.43%
DSN [6] Coarse	82.25 ± 5.91%	90.32%	62.53%

Table 4: Evaluation of different residual connections on the coarse stage of NIH pancreas segmentation.

Method	Mean DSC	Mean Testing Time (s)
ResDSN C2F (Ours)	84.59 ± 4.86%	245
ResDSN Coarse (Ours)	83.18 ± 6.02%	111
ResDSN Fine (Ours)	83.96 ± 5.65%	382

Table 5: Average time cost in the testing phase per case.

we compare four configurations of residual connections of 3D based networks only in the *coarse* stage. The major differences between our backbone network “ResDSN” with respect to “FResDSN”, “SResDSN” and “DSN” are depicted in Table. 1. “ResDSN” outperforms other network architectures in terms of average DSC and a small standard deviation even through the network is not as sophisticated as “FResDSN”, which is the reason we adopt “ResDSN” for efficiency concerns in the *coarse* stage.

5.3. Time Efficiency

We quantitatively discuss the time efficiency of the proposed coarse-to-fine framework with a smaller overlap in the *coarse* stage for the low consuming time concern while a larger one in the *fine* stage for the high prediction accuracy concern. Experimental results are shown in Table 5. “ResDSN Coarse” is the most efficient while the results are the worst among three methods, which makes sense that we care more of the efficiency to obtain a rough pancreas segmentation. “ResDSN Fine” means we use a large overlap on an entire CT scan to do the segmentation which is the most time-consuming. In our coarse-to-fine framework, we combine the two advantages together to propose the “ResDSN C2F” which can achieve the best segmentation results while the average testing time cost for each case is reduced by 36% from 382s to 245s compared with “ResDSN Fine”.

6. Conclusion

In this work, we proposed a novel 3D network called “ResDSN” integrated with a coarse-to-fine framework to simultaneously achieve high segmentation accuracy and low time cost. The backbone network “ResDSN” is carefully designed to only have long residual connections for efficient inference. To our best knowledge, we are the first to segment the challenging pancreas using 3D networks which leverage the rich spatial information to achieve the state-of-the-art. On widely-used datasets, the worst segmentation

case was experimentally improved a lot by our coarse-to-fine framework. What's more, the tendency of giving more under-estimation by 3D coarse network is alleviated by the coarse-to-fine which can gradually refine the hard voxels on the ambiguous boundaries.

In the future, we will target on error causes that lead to inaccurate segmentation to make our framework more stable, and extend our 3D coarse-to-fine framework to pancreatic cyst segmentation which can cause cancerous tumors.

Acknowledgements. We really appreciate the enormous help from Dr. Seyoun Park, Lingxi Xie, Yuyin Zhou, Yan Wang, Fengze Liu, and the very valuable discussions from Qing Liu, Yan Zheng, Chenxi Liu and Zhe Ren.

References

- [1] T. D. Bui, J. Shin, and T. Moon. 3d densely convolution networks for volumetric segmentation. *arXiv:1709.03199*, 2017.
- [2] J. Cai, L. Lu, Y. Xie, F. Xing, and L. Yang. Improving deep pancreas segmentation in CT and MRI images via recurrent neural contextual learning and direct loss function. 2017.
- [3] H. Chen, Q. Dou, L. Yu, J. Qin, and P.-A. Heng. Voxresnet: Deep voxelwise residual networks for brain segmentation from 3d mr images. *NeuroImage*, 2017.
- [4] L.-C. Chen, G. Papandreou, I. Kokkinos, K. Murphy, and A. L. Yuille. Deeplab: Semantic image segmentation with deep convolutional nets, atrous convolution, and fully connected crfs. *arXiv:1606.00915*, 2016.
- [5] Ö. Çiçek, A. Abdulkadir, S. S. Lienkamp, T. Brox, and O. Ronneberger. 3d u-net: learning dense volumetric segmentation from sparse annotation. In *MICCAI*, 2016.
- [6] Q. Dou, L. Yu, H. Chen, Y. Jin, X. Yang, J. Qin, and P.-A. Heng. 3d deeply supervised network for automated segmentation of volumetric medical images. *Medical Image Analysis*, 41:40–54, 2017.
- [7] Y. Fang, J. Xie, G. Dai, M. Wang, F. Zhu, T. Xu, and E. Wong. 3d deep shape descriptor. In *CVPR*, 2015.
- [8] X. Glorot and Y. Bengio. Understanding the difficulty of training deep feedforward neural networks. In *AISTATS*, 2010.
- [9] P. Gravel, G. Beaudoin, and J. A. De Guise. A method for modeling noise in medical images. *IEEE Transactions on medical imaging*, 23(10):1221–1232, 2004.
- [10] M. Havaei, A. Davy, D. Warde-Farley, A. Biard, A. C. Courville, Y. Bengio, C. Pal, P. Jodoin, and H. Larochelle. Brain tumor segmentation with deep neural networks. *Medical Image Analysis*, 35:18–31, 2017.
- [11] K. He, X. Zhang, S. Ren, and J. Sun. Deep residual learning for image recognition. In *CVPR*, 2016.
- [12] S. Ioffe and C. Szegedy. Batch normalization: Accelerating deep network training by reducing internal covariate shift. In *ICML*, 2015.
- [13] Y. Jia, E. Shelhamer, J. Donahue, S. Karayev, J. Long, R. Girshick, S. Guadarrama, and T. Darrell. CAFFE: Convolutional Architecture for Fast Feature Embedding. *ACM MM*, 2014.
- [14] A. Krizhevsky, I. Sutskever, and G. E. Hinton. Imagenet classification with deep convolutional neural networks. In *NIPS*, 2012.
- [15] A. A. Lasboo, P. Rezai, and V. Yaghmai. Morphological analysis of pancreatic cystic masses. *Academic radiology*, 17(3):348–351, 2010.
- [16] C.-Y. Lee, S. Xie, P. Gallagher, Z. Zhang, and Z. Tu. Deeply-supervised nets. In *AISTATS*, 2015.
- [17] J. Long, E. Shelhamer, and T. Darrell. Fully convolutional networks for semantic segmentation. In *CVPR*, 2015.
- [18] J. Merkow, A. Marsden, D. Kriegman, and Z. Tu. Dense volume-to-volume vascular boundary detection. In *MICCAI*, 2016.
- [19] F. Milletari, N. Navab, and S.-A. Ahmadi. V-net: Fully convolutional neural networks for volumetric medical image segmentation. In *3DV*, 2016.
- [20] P. Moeskops, J. M. Wolterink, B. H. M. van der Velden, K. G. A. Gilhuijs, T. Leiner, M. A. Viergeever, and I. Išgum. Deep learning for multi-task medical image segmentation in multiple modalities. *CoRR*, abs/1704.03379, 2017.
- [21] V. Nair and G. E. Hinton. Rectified linear units improve restricted boltzmann machines. In *ICML*, 2010.
- [22] O. Ronneberger, P. Fischer, and T. Brox. U-net: Convolutional networks for biomedical image segmentation. In *MICCAI*, 2015.
- [23] H. R. Roth, L. Lu, A. Farag, H.-C. Shin, J. Liu, E. B. Turkbey, and R. M. Summers. Deeporgan: Multi-level deep convolutional networks for automated pancreas segmentation. In *MICCAI*, 2015.
- [24] H. R. Roth, L. Lu, A. Farag, A. Sohn, and R. M. Summers. Spatial aggregation of holistically-nested networks for automated pancreas segmentation. In *MICCAI*, 2016.
- [25] W. Shen, X. Wang, Y. Wang, X. Bai, and Z. Zhang. Deepcontour: A deep convolutional feature learned by positive-sharing loss for contour detection. In *CVPR*, 2015.
- [26] K. Simonyan and A. Zisserman. Very deep convolutional networks for large-scale image recognition. *arXiv:1409.1556*, 2014.
- [27] B. Stewart, C. P. Wild, et al. World cancer report 2014. *Health*, 2017.
- [28] S. Xie and Z. Tu. Holistically-nested edge detection. In *ICCV*, 2015.
- [29] L. Yu, J.-Z. Cheng, Q. Dou, X. Yang, H. Chen, J. Qin, and P.-A. Heng. Automatic 3d cardiovascular mr segmentation with densely-connected volumetric convnets. In *MICCAI*, 2017.
- [30] L. Yu, X. Yang, H. Chen, J. Qin, and P. Heng. Volumetric convnets with mixed residual connections for automated prostate segmentation from 3d MR images. In *AAAI*, 2017.
- [31] Y. Zhou, L. Xie, E. K. Fishman, and A. L. Yuille. Deep supervision for pancreatic cyst segmentation in abdominal ct scans. In *MICCAI*, 2017.
- [32] Y. Zhou, L. Xie, W. Shen, Y. Wang, E. K. Fishman, and A. L. Yuille. A fixed-point model for pancreas segmentation in abdominal ct scans. In *MICCAI*, 2017.
- [33] Z. Zhu, X. Wang, S. Bai, C. Yao, and X. Bai. Deep learning representation using autoencoder for 3d shape retrieval. *Neurocomputing*, 204:41–50, 2016.

Supplementary Material

In this Section, we show more case examples to illustrate the main difficulties of the pancreas segmentation: 1) the small size of the pancreas in the whole abdominal CT volume; 2) the large variations in the texture, location, shape and size of the pancreas; 3) the significant ambiguities along the boundary between pancreatic and non-pancreatic tissues. We conducted experiments on two datasets, *i.e.*, the NIH pancreas dataset [23] and the JHMI pancreatic cyst dataset [31] in the Experiment Section. Therefore, we illustrate the cases examples from these two datasets, separately.

NIH

In addition to Fig. 1, we illustrate three more cases in the axial, sagittal and coronal views as given in Fig. 6 on the NIH dataset [23]. We can find that the pancreas regions occupy a very small portion of the whole CT volume. The boundaries between different organs are fairly hard to notice. What's more, as shown in Fig. 7, we randomly choose 12 cases from the NIH dataset to illustrate the large variations in the texture, shape and size of the pancreas. Some of the annotated pancreas have smoother boundaries while other annotations are rather jagged, which makes the segmentation task very challenging.

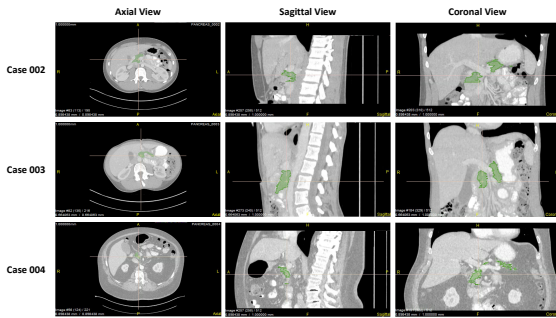


Figure 6: An illustration of three cases from the NIH dataset [23] in terms of three views. Pancreas regions are annotated with green color. Best viewed in color.

JHMI

Different from the NIH dataset, the JHMI pancreatic cyst dataset [31] has pathological pancreas cyst which can be cancerous. Therefore, one major difference between the JHMI dataset and the NIH dataset is that the annotated pancreas regions on the JHMI can contain the pancreatic cyst, which makes the cystic pancreas more difficult to segment than normal cases. As shown in Fig. 8, we select three cases from the JHMI dataset to visualize the pancreas and pancreatic cyst. For the JHMI case 001, the cyst regions occupy most of the pancreas regions while they only take up a very

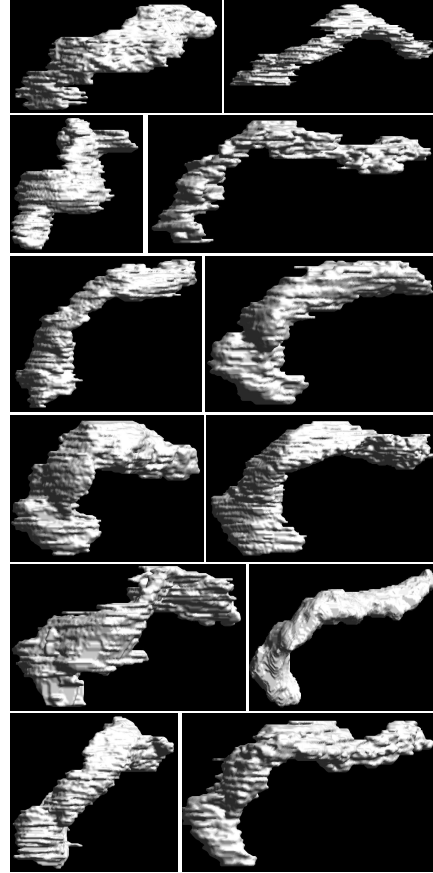


Figure 7: An illustration of 12 pancreas cases from the NIH dataset [23].

small portion of the pancreas regions for other two cases. The large variations of the fraction of cyst with respect to the pancreas make the cystic pancreas segmentation even harder than the normal pancreases.

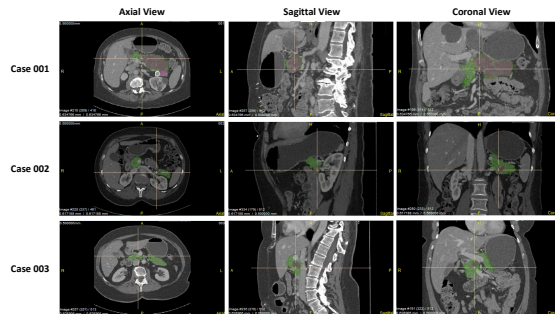


Figure 8: An illustration of three cases from the JHMI dataset [31] in terms of three views. Pancreas regions are annotated with green color while cyst regions are masked as red. Zoom in to see the cyst regions in detail. Best viewed in color.